Proceedings of the ASME 2020
International Design Engineering Technical Conferences
and Computers and Information in Engineering Conference
IDETC/CIE2020
August 17-19, 2020, Virtual, Online

DETC2020-22187

EXAMINE THE BENDING STIFFNESS OF GENERALIZED KRESLING MODULES FOR ROBOTIC MANIPULATION

Joshua Kaufmann and Suyi Li *
Department of Mechanical Engineering
Clemson University, Clemson, SC USA

ABSTRACT

Via analytical modeling and experimental validation, this study examines the bending stiffness adaptation of bistable origami modules based on generalized Kresling pattern. These modules, which are the building blocks of an octopus-inspired robotic manipulator, can create a reconfigurable articulation via switching between their stable states. In this way, the manipulator can exhibit pseudo-linkage kinematics with lower control requirements and improved motion accuracy compared to completely soft manipulators. A key to achieving this reconfigurable articulation is that the underlying Kresling modules must show a sufficient difference in bending stiffness between their stable states. Therefore, this study aims to use both a nonlinear bar-hinge model and experimental testing to uncover the correlation between the module bending stiffness and the corresponding origami designs. The results show that the Kresling origami module can indeed exhibit a significant change in bending stiffness because of the reorientation of its triangular facets. That is, at one stable state, these facets align close to parallel to the longitudinal axis of the cylindrical-shaped module, so the module bending stiffness is relatively high and dominated by the facet stretching. However, at the other stable states, the triangular facets are orientated close to perpendicular to the longitudinal axis, so the bending stiffness is low and dominated by crease folding. The results of this study will provide the necessary design insights for constructing a fully functional manipulator with the desired articulation behavior.

Keywords: Kresling; Robotic Manipulator; Variable Stiffness

1 INTRODUCTION

Soft robots, in contrast to conventional robots, have continuous and compliant bodies due to the softness intrinsic in the underlying materials. This softness provides many advantages in adaptability, resilience, and safety, which make the soft robots ideal for assistive health care, field exploration, and advanced manufacturing applications [1]. Currently, the design, construction, and operating principles of soft robots are extremely diverse [2–4], but many of them take inspiration from examples in nature [5, 6]. The octopus is perhaps the most important source of inspiration because it is capable of performing complex arm movements that enable sophisticated manipulation and locomotion. Several soft robots have been created by mimicking the octopus [7–9]. While these robots have been successful in demonstrating arm manipulations, they usually struggle to achieve a high level of *precision* regarding their arm configuration and movement control. This lack of control precision is due to the severely underactuated nature of continuous and soft robot bodies. That is, the number of embedded actuators in a typical soft robot is far smaller than the kinematic degrees of freedom. Moreover, soft materials exhibit strongly nonlinear visco-elastic properties. As a result, inverse kinematics and overall structure shape are difficult to predict, which makes control tasks such as path planning inaccurate and computationally expensive [10].

One approach to achieving precise control of soft robotic manipulators is to decrease their effective degrees of freedom, and nature again provides terrific examples of this strategy. Sumbre et al. showed that the octopus can generate a quasi-articulated structure in its arm, similar to that of a human, in order to achieve precise point-to-point movement when fetching prey [11] (Figure

*Address all correspondence to this author: suyil@clemson.edu.

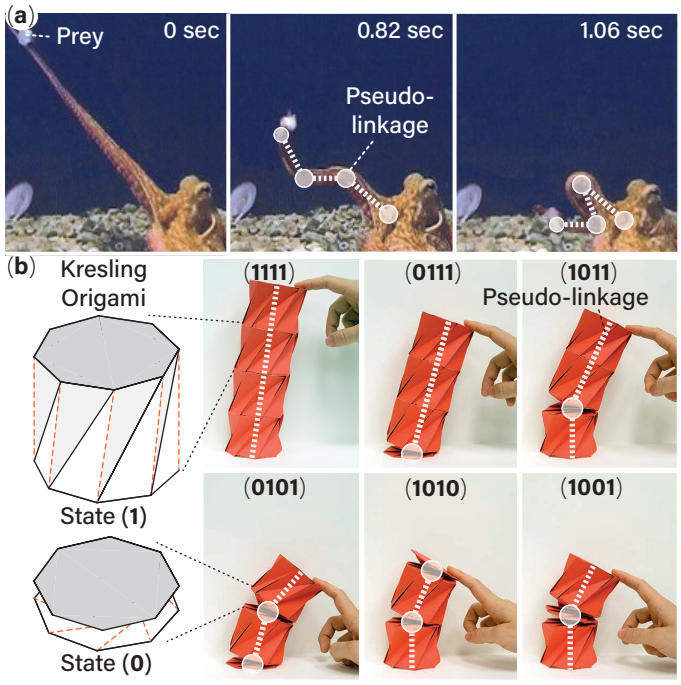

FIGURE 1. Inspiration from nature and the overall concept of this study. (a) The reconfigurable articulation in the octopus arm to achieve rapid prey fetching. Octopus images adapted from [11] with permission. Copyright: Cell Press (b) The bistable Kresling origami cell shows a low bending stiffness at its stable state (0) and higher stiffness at the stable state (1). Therefore, one can exploit this property and create reconfigurable articulation in a robotic manipulator. Notice that stable state distribution is labeled from the base to the tip of this manipulator.

1(a)). The octopus achieves such arm reconfiguration by selectively stiffening sections of its muscles and leaving other sections flexible. Such a reconfigurable structural articulation allows a drastically simplified control by reducing the kinematic degrees of freedom from effectively infinite to a finite amount, thus granting the necessary accuracy to carry out the rapid fetching.

To implement this bio-inspired articulation strategy to a soft robotic manipulator, one must devise a method of localized stiffness adaptation to enable the creation and activation of discrete "joints" at different locations in the robotic arm. To this end, researchers have achieved some success by using jamming-based systems [12], low melting point materials [13], and shape memory materials [14]. However, these methods are limited due to their complexity and scalability [15], as well as the requirement for continuous energy supply to maintain the changes in stiffness.

In order to achieve the localized stiffness adaptation in soft robotic manipulators in a scalable and semi-passive manner, we seek to analyze and exploit the mechanics of a bistable and cylindrical origami known as the Kresling cell. Kresling origami originates from the buckling and collapsing deformation of a cylindrical shell under compression [16], and it has found many applications in morphing structures and locomotion robots [17–20]. More importantly, Kresling can fold between two stable equilibria (or stable states) through a coupled longitudinal and rotational motion [21], and each stable state possesses unique mechanical properties according to its folding geometry. Such bistability can enable binary bending stiffness switching; therefore, we can construct the skeleton of a soft manipulator by serially connecting Kresling cells (or modules). Through strategically switching these Kresling cells between their stable states, we can create joint(s) at any desired location(s), much like the reconfigurable articulation in the octopus arm (Figure 1(b)). This approach is unique in that the localized stiffness adaptation is embodied in the skeleton of the robot itself, and the mechanics are scalable because they are derived primarily from geometry.

A key to implementing this local stiffness adaptation is an understanding of the correlation between Kresling origami cell design and the bending stiffness ratio between its two stable states. Therefore, the objective of this study is to examine the Kresling bending stiffness through both analytical modeling and experimental testing. To this end, the rest of this paper is organized as follows. Section 2 briefly reviews the design of the *generalized* Kresling origami, which is a variation of the classical Kresling pattern to accommodate the kinematic requirement from robotic manipulation. Section 3 details the analytical modeling and experimental testing of the bending stiffness of a Kresling origami module. We employ the nonlinear bar-hinge method developed by Liu and Paulino to examine the bending stiffness ratio between the two stable states [22], and the analytical results agree with three-point bending test results based on paper folded prototypes. Section 4 ends this paper with a summary and discussion of future work. The results of this paper will lay down the foundation for constructing a fully functional soft manipulator with the envisioned reconfigurable articulation.

2 DESIGN OF GENERALIZED KRESLING MODULES

The generalized Kresling consists of a linear array of triangular facets connected by alternating mountain and valley creases (Figure 2). By attaching the two ends of this array, we obtain a twisted polygonal prism with a regular polygon at its top and bottom. A Kresling cell can settle in an extended state (referred to as "state (1)" for simplicity hereafter) or a contracted stable state (aka. "state (0)"). The bistability of Kresling originates from its non-rigid-foldable nature. That is, the triangular facets are flat and undeformed at the two stable states, but must deform during the folding transition between these two states. If these triangular facets were strictly rigid, the Kresling segment would be unable to fold.

Four independent design parameters can fully define the crease pattern of a generalized Kresling cell. They are 1) the

number of polygon sides (N), 2) radius (R), 3) resting length at the contracted stable state ($L_{(0)}$), and 4) an angle ratio (λ). Here, $L_{(0)}$ is the variable that differentiates the generalized Kresling origami from conventional Kresling. The traditional Kresling cell has zero length by definition at the contracted state (a property often known as "flat-foldable"). However, a zero resting length would prevent any kinematic freedom for bending. Therefore, we generalized the Kresling design with a non-zero resting length at state (0) to provide the freedom for bending so that the Kresling cell can work like a revolute "joint" in the pseudo-articulated structure. The angle ratio (λ) influences the strength of the Kresling bistability. The Kresling cell becomes bistable when $0.5 < \lambda < 1$, and the higher the angle ratio, the stronger the bistability becomes in that one needs to apply a higher force to fold the Kresling between two stable states. Interested readers can refer to the authors' previous publication for the detailed differences between generalized and tradition Kresling cell [20].

Once we prescribe the above four design variables, the triangular facets can be defined as

$$D = \sqrt{2R^2\cos^2(\gamma-\lambda\gamma)+L_{(0)}^2}, \tag{1}$$

$$B = \sqrt{P^2+D^2-4PR\cos(\gamma-\lambda\gamma)\cos(\lambda\gamma)}, \tag{2}$$

$$\theta = \cos^{-1}\left(\frac{P^2+D^2-B^2}{2PD}\right), \tag{3}$$

where $\gamma\,(=\pi/2-\varphi)$ is the angle between the diagonal and side of the end polygon, $P\,(=2R\sin\varphi)$ is the end polygon side length, and $\varphi = \pi/N$.

To calculate the resting length of the generalized Kresling cell at its extended stable state (aka. $L_{(1)}$), we first introduce α—the relative rotation angle between the top and bottom end polygon—as the independent variable that describes the folding motion. Moreover, we assume the end polygons are rigid, and the valley creases do not change their length. In this way, facet deformation in the Kresling cell during folding can be approximated by the shortening of mountain creases [20], and we can calculate the mountain crease length as well as the overall Kresling cell length as functions of α:

$$l(\alpha) = \sqrt{L_{(0)}^2+2R^2\left[\cos(\alpha+2\varphi)-\cos(\alpha_{(0)}+2\varphi)\right]}, \tag{4}$$

$$b(\alpha) = \sqrt{2R^2(1-\cos(\alpha))+l^2}. \tag{5}$$

Here, $\alpha_{(0)}\ (=2\lambda\gamma)$ is the angle between top and bottom polygon at the contracted stable state (0). $\alpha_{(1)}$ corresponding to the extended stable state (1) and it can be computed as:

$$\alpha_{(1)} = 2(1-\lambda)\gamma,\ \ \forall\,\lambda > 0.5. \tag{6}$$

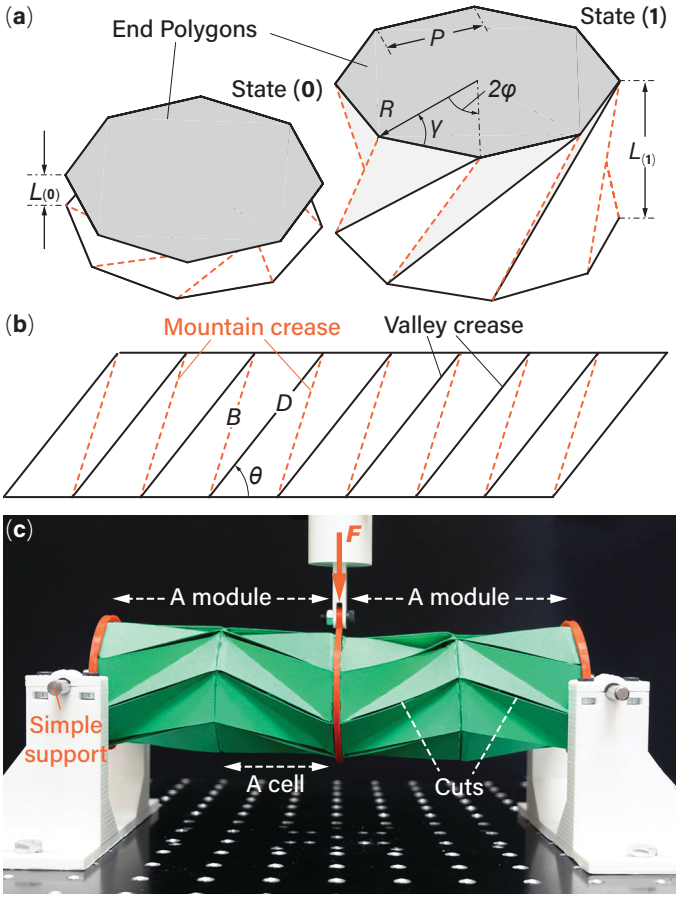

FIGURE 2. Design of the generalized Kresling origami cell and the module. (a) The external geometry of the generalized Kresling cell at its two stable states. (b) The corresponding crease pattern. (c) The three-point bending test setup in this study. The test involves a dual-module assembly, and each module consists of two Kresling cells of the opposite chirality. Notice that the mountain creases of Kresling cells are cut open to avoid excessive deformation during the switch between two stable states.

Based on the equations above, one can fully determine the external geometry of the generalized Kresling origami cell at its two different stable states, which will be used in the nonlinear bar-hinge analysis discussed in the section below.

3 ANALYZING THE KRESLING BENDING STIFFNESS

To quantitatively examine the bending stiffness of Kresling cell at its two stable states, we use both analytical modeling based on the nonlinear bar-hinge model and experimental validation. A single Kresling cell defined in Figure 2 shows twisting in addition to longitudinal deformation when it folds from one stable state to the other, and this twisting is undesirable for the robotic manipulation purpose. Therefore, we define a Kresling "mod-

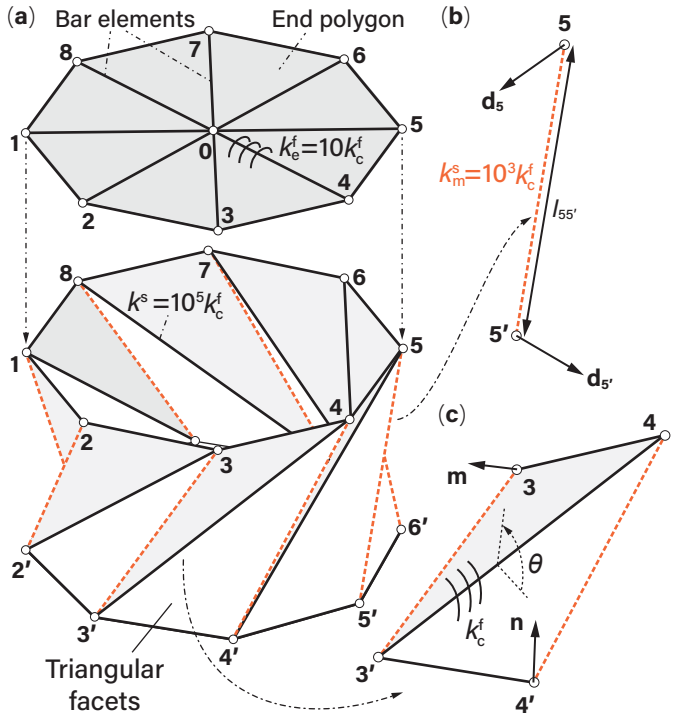

FIGURE 3. Fundamentals of the nonlinear bar-hinge method using a Kresling cell as an example. (a) The Kresling cell, after being transformed into an equivalent pin-jointed truss-frame system. Here, solid and dashed lines represent stretchable bar elements, and hollow circles represent pin-joints. Notice that the end polygons are divided into N triangles. (b) The kinematics of a bar element. (c) The kinematics of a dihedral folding angle θ that describes the folding between two triangular facets. Compared to the valley creases (solid lines), the mountain creases between the triangular facets (dashed lines) have relatively lower axial rigidity and zero folding stiffness due to the cut shown in Figure 2(c).

ule" by combing two kresling cells of the same design but opposite chirality (Figure 2(c)). In this way, the two end polygons of a module would not rotate with respect to each other. The bending stiffness of the Kresling module is then defined based on the transverse deformation of a dual-module assembly when it is subject to a concentrated force at its center point, similar to a three-point bending test (Figure 2(c)). The following subsections detail the modeling and experimental setup of this three-point bending test, while the third subsection discusses the results.

3.1 Establishing The Nonlinear Bar-Hinge Model

The bar-hinge model transforms the continuous origami into a pin-jointed truss-frame structure by using elastic bar elements to represent the creases (Figure 3(a)). This reduced-order model is capable of analyzing the folding kinematics and principle deformations of different origamis without incurring expensive computational cost like in the finite element simulations [22–25]. In this study, we use the nonlinear bar-hinge models developed by Liu and Paulino to analyze the bending stiffness of the dual-module Kresling origami assembly. Here, we briefly discuss the fundamentals of this model, and interested readers can refer to the previous literature for more technical details [22].

The overall stiffness of the bar-hinge system has two components. One comes from the stretching of the bar elements and the other from the folding (or bending) between adjacent triangular facets. The bar stretching stiffness represents the in-plane stretching and shearing stiffness of the sheet material in Kresling modules. Using the bar element connecting pin-joints 5 and 5' as an example (Figure 3(b)), one can define $\mathbf{u}_{55'} = \left[\mathbf{d}_5^{\mathsf{T}} \ \mathbf{d}_{5'}^{\mathsf{T}}\right]^{\mathsf{T}}$, where $\mathbf{d}_5$ and $\mathbf{d}_{5'}$ are the displacement vector of the pin joint #5 and #5', respectively. $l_{55'}$ is the length of this bar element. The Green-Lagrangian strain of this bar element is

$$\varepsilon_{55'} = \mathbf{B}\mathbf{u}_{55'} + \frac{1}{2}\mathbf{u}_{55'}^{\mathsf{T}}\mathbf{D}\mathbf{u}_{55'}, \tag{7}$$

where

$$\mathbf{B} = \frac{1}{l_{55'}}\left[-\mathbf{e} \ \ \mathbf{e}\right], \tag{8}$$

$$\mathbf{D} = \frac{1}{l_{55'}^2}\begin{bmatrix} \mathbf{I}_{3\times3} & -\mathbf{I}_{3\times3} \\ -\mathbf{I}_{3\times3} & \mathbf{I}_{3\times3} \end{bmatrix}. \tag{9}$$

Here, $\mathbf{e} = [1 \ \ 0 \ \ 0]$, and $\mathbf{I}_{3\times3}$ is the identify matrix of size 3×3. The tangent stiffness matrix components corresponding to this bar element are

$$\mathbf{K}_{55'}^{(\mathrm{bar})} = k_{55'}^{\mathrm{s}} l_{55'}\left(\mathbf{B}^{\mathsf{T}} + \mathbf{D}\mathbf{u}_{55'}\right)\left(\mathbf{B}^{\mathsf{T}} + \mathbf{D}\mathbf{u}_{55'}\right)^{\mathsf{T}} + f_{55'} l_{55'}\mathbf{D}, \tag{10}$$

where $k_{55'}^{\mathrm{s}}$ is the axial rigidity of this bar element, and $f_{55'}$ is the resultant longitudinal force. It is worth noting that this stiffness matrix involves both the linear term and nonlinear terms related to geometry and initial displacement [22]. One can then apply similar formulations to all bar elements and assemble the global bar stiffness matrix.

Besides bar stretching, folding and bending between the adjacent triangular facet are also crucial sources of stiffness. Here, the creases behave like hinges with prescribed torsional spring stiffness. Using the valley crease defined by pin-joints #3' and #4 as an example, one can calculate the dihedral angle between the two adjacent facets based on their surface normal vectors (e.g., $\mathbf{m}$ and $\mathbf{n}$ in Figure 3(c)) so that

$$\theta = \eta\cos^{-1}\left(\frac{\mathbf{m}\cdot\mathbf{n}}{\|\mathbf{m}\|\|\mathbf{n}\|}\right), \tag{11}$$

where the surface normal vectors $\mathbf{m} = \mathbf{r}_{33'} \times \mathbf{r}_{43'}$, $\mathbf{n} = \mathbf{r}_{43'} \times \mathbf{r}_{44'}$, and η is a sign indicator in that

$$\eta = \begin{cases} \text{sgn}(\mathbf{m} \cdot \mathbf{r}_{43'}) & \text{if } \mathbf{m} \cdot \mathbf{r}_{43'} \neq 0; \\ 1 & \text{if } \mathbf{m} \cdot \mathbf{r}_{43'} = 0. \end{cases} \tag{12}$$

The elements of tangent stiffness matrix corresponding to this dihedral angle are are defined as

$$K_{3'4}^{(\text{fold})} = k_{3'4}^{\text{f}} l_{3'4} \frac{\mathrm{d}\theta}{\mathrm{d}\mathbf{x}} \otimes \frac{\mathrm{d}\theta}{\mathrm{d}\mathbf{x}} + m_{3'4} \frac{\mathrm{d}^2\theta}{\mathrm{d}\mathbf{x}^2}, \tag{13}$$

where $\otimes$ is tensor product, $l_{3'4}$ is the crease length corresponding to this dihedral angle, $k_{3'4}^{\text{f}}$ is the torsional spring stiffness *per unit length* of this crease, $m_{3'4}$ is the resultant torque, and $\mathbf{x}$ is the position vector of the related pin-joints at the current configuration.

In this study, we assume the axial bar rigidity k^{s} and crease torsional stiffness per unit length k^{f} are all constant so that the Kresling module nonlinearity originates from the finite-amplitude deformation during folding. Moreover, the values of k^{s} and k^{f} are different in different parts of the Kresling module. The torsional spring stiffness per unit length of the origami creases k_{c}^{f}—including the valley creases on the side (e.g., 2'3 and 3'4) as well as the creases between end polygons and triangular facets (e.g., 23 and 2'3')—are experimentally measured (as we detail in subsection 3.2 below). The torsional stiffness in the end polygons k_{e}^{f} (e.g., along 01 and 02) is assumed to be an order of magnitude higher than the valley crease stiffness because they represent the polygon material bending ($k_{\text{e}}^{\text{f}} = 10k_{\text{c}}^{\text{f}}$). However, the torsional spring stiffness of the mountain creases (e.g., 22' and 33') is zero due to the cuts (Figure 2(c)). Moreover, we assume the same axial rigidity for all bar elements in that $k^{\text{s}} = 10^5 k_{\text{c}}^{\text{f}}$, except for the bar elements along the mountain creases between the triangular facets. The axial rigidity of these mountain crease bar elements is two orders of magnitude lower than the valley crease bar elements due to the cuts (aka. $k_{\text{m}}^{\text{s}} = 10^3 k_{\text{c}}^{\text{f}}$).

After setting up the bar-hinge model and applying boundary conditions according to the three-point bending test, we use the MERLIN2 software[1] to simulate the bending deformation of a dual-module Kresling structure under a transverse load. The results are summarized in subsection 3.3.

3.2 Experimental Testing

In this study, we performed two different sets of experiments. One aims to estimate the torsional stiffness of paper creases k_{c}^{f}, which is required for the nonlinear bar-hinge model, as mentioned in the previous Section 3.1. The other three-point-bending test directly measures the bending stiffness of the Kresling module at its two different stable states. Here, we briefly discuss the experimental setup.

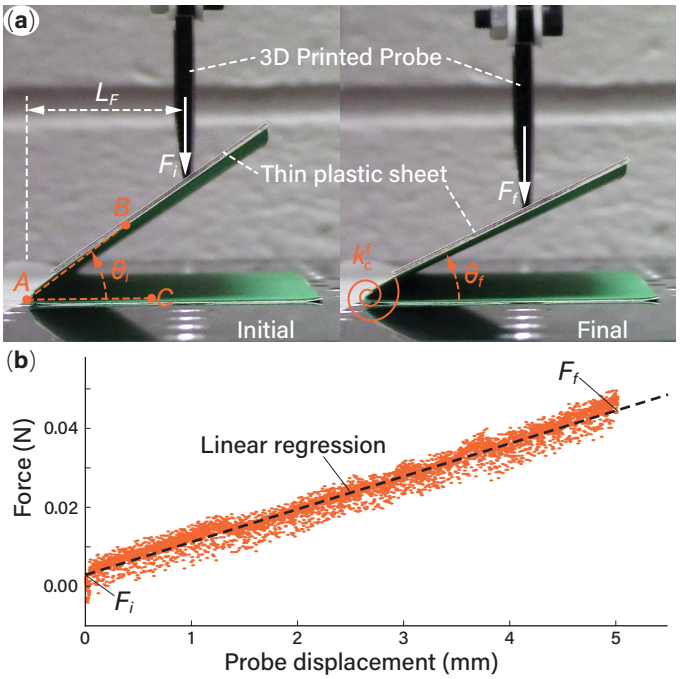

FIGURE 4. Experimental setup for measuring the crease torsional spring stiffness per unit length (k_{c}^{f}). (a) Screenshots for the video footage that shows the course of these tests. (b) A set of force-displacement data that shows a close-to-linear behavior.

Crease stiffness test: We experimentally measure the crease torsional stiffness k_{c}^{f} for the nonlinear bar-and-hinge model by using paper-based, hinge-like samples consisting of two 15.24 cm by 4.45 cm rectangular facets connected by a perforated crease (Figure 4). The creases are fabricated on a Cricut Maker™ cutter plotter. We reinforce the upward-facing facet with a thin plastic sheet to eliminate panel bending and secure the bottom facet to the base plate of an ADMET eXpert™ 5601 universal testing machine with double-sided tape. A 3D-printed, wedge-shaped probe is used to distribute compressive forces evenly across the upward facet (Figure 4(a)).

Before carrying out each test, we place the samples under a slight compressive load to ensure sufficient contact between the probe and sample. Then, a controlled probe displacement of 5mm deforms the samples in the downward vertical direction (Figure 4(a)). We take high-resolution videos of the deformed samples during these tests and use MATLAB image processing tools to measure the sample deformation. More specifically, we extract the first and last frames from the videos to represent the

[1]This software is available as a MATLAB package at www.paulino.ce.gatech.edu/software.html

starting and ending configurations, respectively. Then we manually select the crease vertex point A, a point B on the upward facet, and a point C on the downward facet and then retrieve their respective x and y coordinates using image processing program (Figure 4(a)). In this way, we can calculate the distance between these points and the corresponding dihedral folding angle θ:

$$\theta = \cos^{-1}\left(\frac{L_{AB}^2 + L_{AC}^2 - L_{BC}^2}{2L_{AC}L_{AB}}\right) \tag{14}$$

The measured force-displacement curve is close to linear (Figure 4(b)). Therefore, we performed a linear regression to the data to estimate the initial force F_i and final external force F_f, respectively. In this way, the linear crease torsional spring stiffness *per unit length* can be estimated as

$$k_c^f = \frac{L_F \cos\theta_i \left(F_f - F_i\right)}{W\|\theta_i - \theta_f\|}, \tag{15}$$

where θ_i and θ_f are the initial and final dihedral angles, respectively. L_F is the distance from the crease vertex to the applied force, and W is the width of this crease sample. We fabricated five identical samples and conducted three load cycles on each sample. The measured crease torsional stiffness per unit length is $k_c^f = 0.047 \pm 0.011$ N/rad. The averaged k_c^f value is used in the nonlinear bar-hinge model.

Kresling module stiffness test: To experimentally validate the bending stiffness adaptation of the Kresling modules between their two stable states, we fabricated a paper-based prototype and conducted a three-point bending test (Figure 2(c) and 5). To fabricate a Kresling cell, we first create the Kresling geometry in a CAD program and convert it into a vectorized image file. This file is then sent to a cutter plotter (Graphtec FCX4000-50ES) that can accurately perforate the crease lines and cut the Kresling cells out of a large piece of thick paper (Daler-Rowney Canford 150 gsm). We then manually fold these cells and assemble them into Kresling modules for testing. It is worth noting that the Kresling cells have cuts along the mountain creases to alleviate stresses that lead to tearing. Also, the triangular facets have reinforcement panels pasted inside to increase their bending stiffness, thus increasing the bistability strength [20].

To set up the three-point bending test, we attach the two Kresling modules to a 3D-printed fixture, which provides a connection to the crosshead of the universal testing machine. Another set of 3D-printed end caps are then attached to the other end of each module to provide hinge support. Customize-designed, 3D-printed end fixtures provide the connection to the base plate of the universal testing machine (Figure 5).

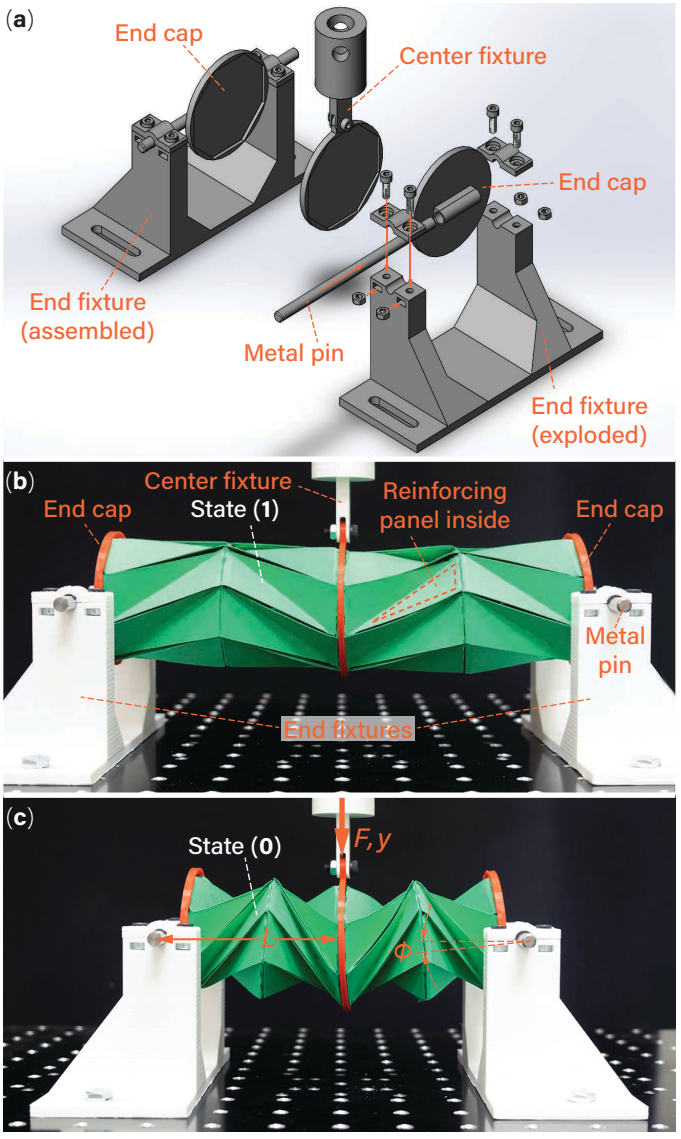

FIGURE 5. Experimental setup for measuring the bending stiffness of the Kresling module. (a) CAD models illustrating the design of the various fixtures for the three point bending test. (b) Bent Kresling modules at their stable state (1). (c) Bent Kresling modules at state (0).

The completed assembly is then secured to the universal testing machine and fixed at either their extended (1) or compressed (0) state (Figure 5(b,c)). We then apply a 5mm downward displacement at a rate of 0.1mm/sec. In this way, the effective bending stiffness of a Kresling module is

$$K_B = \frac{M}{\phi} = \frac{FL}{\tan^{-1}(y/L)}, \tag{16}$$

TABLE 1. Kresling design parameters used in this test, the definition of these parameters are detailed in Section 2.

Parameter	Value
N	8
λ	0.8
$L_{(0)}$	30 mm
R	30 mm

where M is the applied moment, ϕ is the rotation angle, F is the reaction force, y is the downward displacement, and L is distance between applied force and rotation axis of the Kresling module.

3.3 Results and Discussions

Figure 6 summarizes the results of Kresling module bending stiffness, both from the nonlinear bar-hinge model and three-point bending tests, and the corresponding Kresling design parameters are listed in Table 1. Based on the results, one can observe a significant difference in bending stiffness between the two stable states. Compared to the bar-hinge model predictions, the experimental results show a stronger nonlinearity at the beginning of the load cycles. This discrepancy probably originates from the fact that the Kresling module prototypes have to be compressed slightly before testing so that their initial length L equals to the theoretically predicted resting length at the two stable states (aka. $L = L_{(0)}$ or $L_{(1)}$). This small compression would generate some initial stress in the structure. Regardless, the Kresling samples show a close-to-linear behavior as the bending angle θ increases, and the analytical and experimental results agree well with each other in terms of the *slope* of these moment-angle curves, which is the performance metric used for this study. The ratio of bending stiffness at stable state (1) over the state (0) is 5.83 based on the nonlinear bar-hinge analysis and 5.06 based on the experiment. To obtain more accurate predictions, one can improve the nonlinear bar-hinge model to include pre-stress, especially along the creases. Some additional testing on the facet bending stiffness is also beneficial.

Careful inspection of the Kresling origami geometry can reveal the physical principles that underpin this stiffness change. At the extended state (1), the triangular facets in the Kresling origami align close to parallel to the longitudinal axis of the cylindrical-shaped module, so the overall bending stiffness is relatively high and dominated by the facet stretching. However, at the contracted state (0), the triangular facets are orientated close to perpendicular to the longitudinal axis, so the bending stiffness is low and dictated by the crease folding.

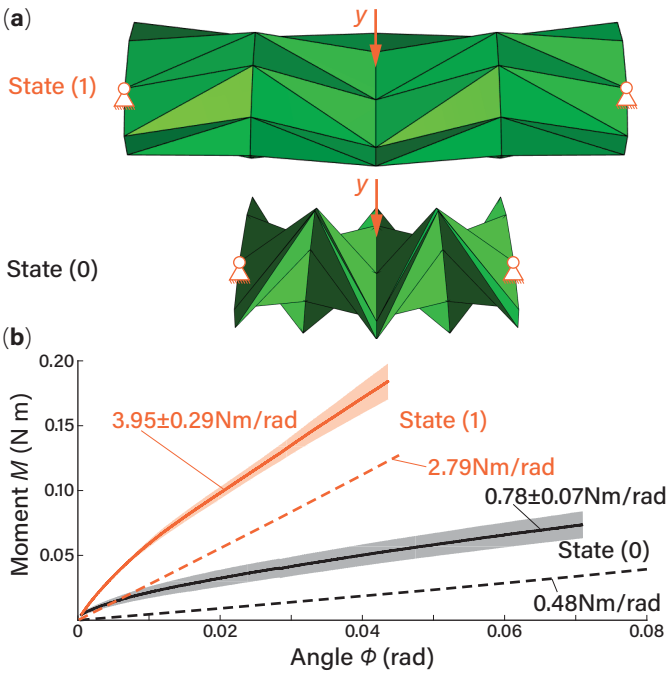

FIGURE 6. Results on the Kresling module bending stiffness: a) The simulated bending of the dual module assembly based on the nonlinear bar-hinge model. b) The moment-rotation relationship according to Equation 16. Here, the dashed lines are the bar-hinge model prediction, the solid lines are the averaged test results based on three loading cycles, and shaded bands are the corresponding standard deviation.

4 SUMMARY AND CONCLUSIONS

This study investigates the bending stiffness adaptation of bistable origami modules based on a generalized Kresling pattern. Due to the reorientation of its triangular facets via folding, a Kresling module can show a significant difference in bending stiffness between its two stable states. That is, at the extended stable state (1), the module bending stiffness is relatively high and dominated by in-plane facet stretching. However, at the contracted state (0), the bending stiffness is low and dictated by the crease folding. By using a nonlinear bar-hinge model with experimental validation, we establish a quantitative correlation between this bending stiffness adaptation and Kresling design parameters. A proof-of-concept Kresling module design manages to provide a bending stiffness ratio of 5.83 according to model prediction and 5.06 according to experimental testing.

The results of this study prove that the concept of reconfigurable articulation in a continuous manipulator—as envisioned in Figure 1—is indeed feasible. Moreover, they provide the necessary analytical and experimental tools for fine-tuning the generalized Kresling design according to the kinematics and other performance requirements for such robotic applications. There-

fore, this study paves the way for constructing a fully-functional robotic manipulator. In the follow up study, we plan to use the numerical and experimental methods established in this study to identify the optimal Kresling origami design, construct a functional robotic arm with multiple Kresling modules, and then analyze its kinematics performance based on the reconfigurable articulation.

ACKNOWLEDGMENT

The authors acknowledge the support from Clemson University (via startup fund and CECAS Dean's Faculty Fellow Award) and National Science Foundation (CMMI-1751449 CAREER, and 1933124).

REFERENCES

[1] Rus, D., and Tolley, M. T., 2015. "Design, fabrication and control of soft robots". *Nature,* ***521***(7553), pp. 467–475.

[2] Laschi, C., Mazzolai, B., and Cianchetti, M., 2016. "Soft robotics: Technologies and systems pushing the boundaries of robot abilities". *Science Robotics,* ***1***(1), p. eaah3690.

[3] Rich, S. I., Wood, R. J., and Majidi, C., 2018. "Untethered soft robotics". *Nature Electronics,* ***1***(2), pp. 102–112.

[4] Whitesides, G. M., 2018. "Soft Robotics". *Angewandte Chemie International Edition,* ***57***(16), pp. 4258–4273.

[5] Trivedi, D., Rahn, C. D., Kier, W. M., and Walker, I. D., 2008. "Soft robotics: Biological inspiration, state of the art, and future research". *Applied Bionics and Biomechanics,* ***5***(3), pp. 99–117.

[6] Kim, S., Laschi, C., and Trimmer, B., 2013. "Soft robotics: A bioinspired evolution in robotics". *Trends in Biotechnology,* ***31***(5), pp. 287–294.

[7] Laschi, C., Cianchetti, M., Mazzolai, B., Margheri, L., Follador, M., and Dario, P., 2012. "Soft robot arm inspired by the octopus". *Advanced Robotics,* ***26***(7), pp. 709–727.

[8] McMahan, W., Chitrakaran, V., Csencsits, M., Dawson, D., Walker, I. D., Jones, B. A., Pritts, M., Dienno, D., Grissom, M., and Rahn, C. D., 2006. "Field trials and testing of the OctArm continuum manipulator". *Proceedings - IEEE International Conference on Robotics and Automation,* ***2006***(May), pp. 2336–2341.

[9] Calisti, M., Giorelli, M., Levy, G., Mazzolai, B., Hochner, B., Laschi, C., and Dario, P., 2011. "An octopus-bioinspired solution to movement and manipulation for soft robots". *Bioinspiration and Biomimetics,* ***6***(3).

[10] George Thuruthel, T., Ansari, Y., Falotico, E., and Laschi, C., 2018. "Control Strategies for Soft Robotic Manipulators: A Survey". *Soft Robotics,* ***5***(2), p. soro.2017.0007.

[11] Sumbre, G., Fiorito, G., Flash, T., and Hochner, B., 2006. "Octopuses Use a Human-like Strategy to Control Precise Point-to-Point Arm Movements". *Current Biology,* ***16***(8), pp. 767–772.

[12] Cheng, N. G., Lobovsky, M. B., Keating, S. J., Setapen, A. M., Gero, K. I., Hosoi, A. E., and Iagnemma, K. D., 2012. "Design and Analysis of a Robust, Low-cost, Highly Articulated Manipulator Enabled by Jamming of Granular Media". *Proceedings of 2012 IEEE International Conference on Robotics and Automation (ICRA)*, pp. 4328–4333.

[13] Cheng, N., Ishigami, G., Hawthorne, S., Chen, H., Hansen, M., Telleria, M., Playter, R., and Iagnemma, K., 2010. "Design and analysis of a soft mobile robot composed of multiple thermally activated joints driven by a single actuator". *Proceedings - IEEE International Conference on Robotics and Automation*, pp. 5207–5212.

[14] Firouzeh, A., Mirrazavi Salehian, S. S., Billard, A., and Paik, J., 2015. "An under actuated robotic arm with adjustable stiffness shape memory polymer joints". *Proceedings - IEEE International Conference on Robotics and Automation,* ***2015-June***, pp. 2536–2543.

[15] Manti, M., Cacucciolo, V., and Cianchetti, M., 2016. "Stiffening in soft robotics: A review of the state of the art". *IEEE Robotics and Automation Magazine,* ***23***(3), pp. 93–106.

[16] Hunt, G. W., and Ario, I., 2005. "Twist buckling and the foldable cylinder: An exercise in origami". *International Journal of Non-Linear Mechanics,* ***40***(6), jul, pp. 833–843.

[17] Jianguo, C., Xiaowei, D., Ya, Z., Jian, F., and Yongming, T., 2015. "Bistable behavior of the cylindrical origami structure with kresling pattern". *Journal of Mechanical Design,* ***137***(6), p. 061406.

[18] Nayakanti, N., Tawfick, S. H., and Hart, A. J., 2017. "Twist Coupled Kirigami Cellular Metamaterials and Mechanisms". *Extreme Mechanics Letters*.

[19] Pagano, A., Yan, T., Chien, B., Wissa, A., and Tawfick, S., 2017. "A crawling robot driven by multi-stable origami". *Smart Materials and Structures,* ***26***(9), p. 094007.

[20] Bhovad, P., Kaufmann, J., and Li, S., 2019. "Peristaltic locomotion without digital controllers: Exploiting multi-stability in origami to coordinate robotic motion". *Extreme Mechanics Letters,* ***32***, p. 100552.

[21] Pagano, A., Yan, T., Chien, B., Wissa, A., and Tawfick, S., 2017. "A crawling robot driven by multi-stable origami". *Smart Materials and Structures,* ***26***(9).

[22] Liu, K., and Paulino, G. H., 2017. "Nonlinear mechanics of non-rigid origami: an efficient computational approach". *Proceedings of the Royal Society A: Mathematical, Physical and Engineering Science,* ***473***(2206), oct, p. 20170348.

[23] Schenk, M., and Guest, S. D., 2013. "Geometry of Miura-folded metamaterials". *Proceedings of the National Academy of Sciences,* ***110***(9), feb, pp. 3276–3281.

[24] Li, S., and Wang, K. W., 2015. "Fluidic origami: a plant-inspired adaptive structure with shape morphing and stiff-

ness tuning". *Smart Materials and Structures,* ***24***(10), p. 105031.

[25] Gillman, A., Fuchi, K., and Buskohl, P., 2018. "Truss-based nonlinear mechanical analysis for origami structures exhibiting bifurcation and limit point instabilities". *International Journal of Solids and Structures,* ***147***, pp. 80–93.